Characterization of eddy scales over tandem obstacles for surface wave-dominated flow

Krishnendu Barman[1,*], Sayahnya Roy[2] and Koustuv Debnath[2]

[1]Applied Mathematics with Oceanology and Computer Programming, Vidyasagar University, Paschim Medinipur 721 102, India
[2]Department of Aerospace Engineering and Applied Mechanics, Indian Institute of Engineering Science and Technology, Shibpur 711 103, India

The present experimental study was performed to explain the effects of the couple interaction between wave and current over a pair of hemispheres. Probability density function for the velocity fluctuation was analysed to explore the response of a surface wave on the following current. The external forcing effects of the hemisphere and superimposed surface waves within the main flow field are capable of modulating the entire range of turbulent eddy scales, and have an essential role in the modulation of the distribution of different eddy scales in the frequency domain.

Keywords: Bursting event, eddy scales, probability density function, surface waves, wavelet analysis.

THE impact of tidal waves on shallow-water river flows in the estuaries is important in coastal zone management. The combined wave–current interaction over two inline hemispheres has a complex flow structure, which may affect the nearshore underwater biological processes. The shallow tidal zone around an island is characterized by a flow environment similar to that tested in this study. The turbulent structures can transform the surrounding flow environment and generate flow microhabitats. Ferrier and Carpenter[1] reported that the algal communities within the wake region of the reef were found to have a large cover of foliose red algal species. This indicates that the turbulent flow environment can modify the morphology of algal species. Furthermore, the turbulence produced from organisms (such as shells, different types of phytoplankton, mussels, various types of pebbles, etc.) themselves propagates upward and turbulence is propagated downwards due to waves from the surface. However, these complex interactions modify the turbulence flow field near the bottom wall, thus altering the behavioural pattern of organisms in wave-dominated regions. Therefore, it is an important factor for these submerged alluvial species and their hydrological processes in wave–current environment. The present study is of significance for improved management of the marine biological processes, specifically evaluation of pipeline scour in many aquatic channels such as sea- or river-bed, control of bank erosion, assessment of the spreading of pollutants, marine engineering applications, and several coastal and continental environments such as estuaries, lower shoreface and surf zone.

Laboratory experiments based on wave–current interacting flow have been carried out by several researchers[2–4]. These studies showed that both the Reynolds shear stress and turbulence intensity increased in magnitude due to the coexistence of current and surface waves of different frequency for flow over a plane bed. It is important to recognize that turbulence level of streams, rivers, seas, lakes and estuaries control the different physiochemical characteristics of maritime environment which in turn govern the migration characteristics of biological communities. Nikora *et al.*[5] performed an experimental study of the turbulence properties of the flow field, which modulated the growth of microorganisms over the flume bed. Agelinchaab and Tachie[6] demonstrated that the mean flow and turbulence features change considerably at the cavity of roughness for their study over hemispherical ribs using a particle image velocimetry (PIV).

Recently, wavelet transform techniques have attracted attention for analysing the random velocity signal to characterize the structure of eddies initiated from bottom roughness for wave–current flow interaction. Wavelet analysis is capable of resolving a signal in both time and frequency domain allowing a closer inspection of a signal in resolving association between the function and its individual coefficients. Wavelet techniques have been employed in several studies to assess the turbulent velocity signal of turbulent flow field[7–10]. However, continuous wavelet transform is an important tool to recognize the characteristics of the turbulence eddy formation and its structures[7]. Further, to identify the coherent flow structures, discrete orthonormal wavelet transformation was utilized on turbulence quantifications[8]. Wang *et al.*[10] represented the wavelet interpretations of instantaneous velocity signal which is accomplished for supplying knowledge on size of eddy scale and their frequency of occurrence.

In spite of these previous studies, no work reported the distribution of velocity vectors and the characteristics of eddy scales for the interaction of wave–current flow cases over two inline hemispheres. In this study, the distribution of probability density function (PDF) is discussed in detail for obtaining the oscillation patterns that affect

*For correspondence. (e-mail: krishnendubarman07@gmail.com)

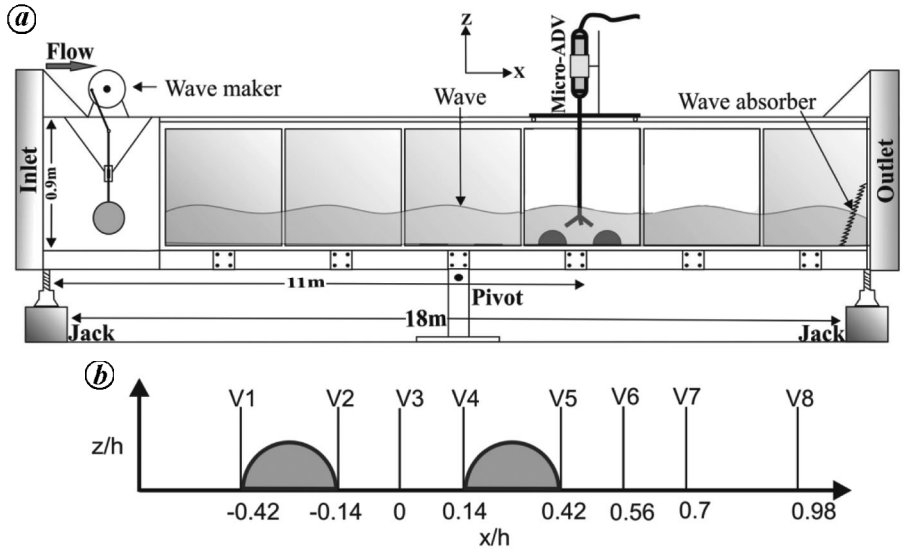

Figure 1. (***a***) Schematic representation of the experimental set-up and (***b***) detailed illustration of measurement sections.

the turbulent properties in the complex environment created by the current, waves and bottom-wall roughness interactions. Therefore, flow structure in the presence of submerged hemispheres and their sheltering effects are essential to characterize the turbulence properties and coherent eddy structures within the background superimposed surface wave environments.

Experiments

A series of experiments were conducted in a wave–current tilting flume (Figure 1). A 16 MHz micro-acoustic Doppler velocimeter (ADV) was mounted on the flume to collect the instantaneous velocity time series along the centreline of the channel. Details of the experimental set-up including the wave-maker (Figure 1 *a*) and its functioning are similar to those of Barman *et al.*[11]. Sampling volume of the ADV is located approximately 5 cm away from the transmitter probe. Sampling volume of nearly cylindrical shape is aligned along the transmitter beam axis of diameter 0.6 cm, and 0.32 cm length with a sampling volume of approximately 0.09 cm^3. Further, factory calibration of the ADV was ±1.0% of the collected velocity time-series (i.e. a precision of ±1 cm/sec for an acquired velocity of 100 cm/sec). The velocity data were 'cleaned' by removing all announcement errors to maintain the signal-to-noise ratio in the range less than 15 dB, whereas correlation samples were below 70%. The filtering procedure was executed using Win-ADV software, ensuing in the elimination of 1.8% of all measured instantaneous velocity data. The uncertainty analysis has been performed in detail in previous studies[12,13].

In this study, the hemisphere radius (R) was 2.8 cm and pitch distance (centre-to-centre spacing) between the two hemispheres was 11.2 cm. Before the experimental run, eight distinct stream-wise measuring points V1 to V8 were marked at the centreline on the bottom wall over the tandem hemispheres (Figure 1 *b*) to characterize the turbulence statistics under uniform flow conditions. The present experimental run was conducted using identical flow parameters are follows: mean water depth $h = 20$ cm, slope of flume bed = 0.00025, depth-averaged mean velocity $U = 29.4$ cm/sec, Reynolds number R_e ($=Uh/\nu$) = 5.88×10^4 and Froude number F_r ($= U/(gh)^{0.5}$) = 0.21, where ν is the kinematic viscosity of the fluid and g is the gravitational force. The apparent wavelength L_w (65 and 35 cm for $f = 1$ and 2 Hz respectively) and wave height h_w (2.0 and 3.1 cm for $f = 1$ and 2 Hz respectively) were recorded using the camera at different sections of the wave–current flume.

Results and discussion

The instantaneous longitudinal, transverse and wall-normal velocity components (u, v and w respectively) are interrelated with the time-averaged ($\overline{u}, \overline{v}, \overline{w}$) and fluctuating ($u'$, v', w') components along the three-dimensional coordinate axes (x, y, z) and expressed as

$$u(t) = \overline{u} + u', \; v(t) = \overline{v} + v', \; w(t) = \overline{w} + w'. \tag{1}$$

The longitudinal mean velocity for hydraulically rough wall surface of channel was used in the standard log-law equation as

$$\overline{u}/u_* = 1/\kappa \ln(z/z_0), \text{ with } z_0 = k_s/30, \tag{2}$$

where κ and k_s are the von Karman constant (≈0.40) and wall roughness height (≈0.042 cm) respectively, along with a regression coefficient $R^2 \approx 0.96$. The friction velocity u_* (= 1.4 cm/s) and wall roughness height k_s

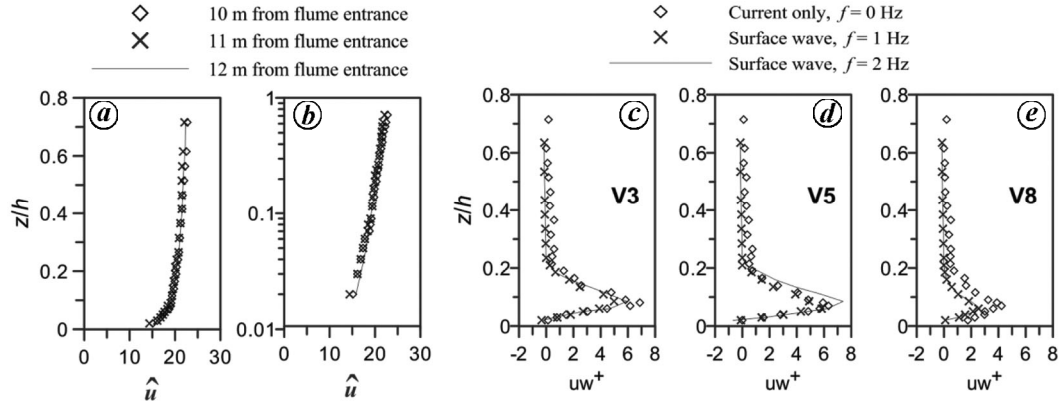

Figure 2. Normalized distribution of (***a***) longitudinal mean velocities ($\hat{u}$), (***b***) longitudinal mean velocity in log scale at 10, 11 and 12 m from the flume entrance, and (***c***–***e***) Reynolds shear stress (uw^+) for V3, V5 and V8 (Figure 1 *b*).

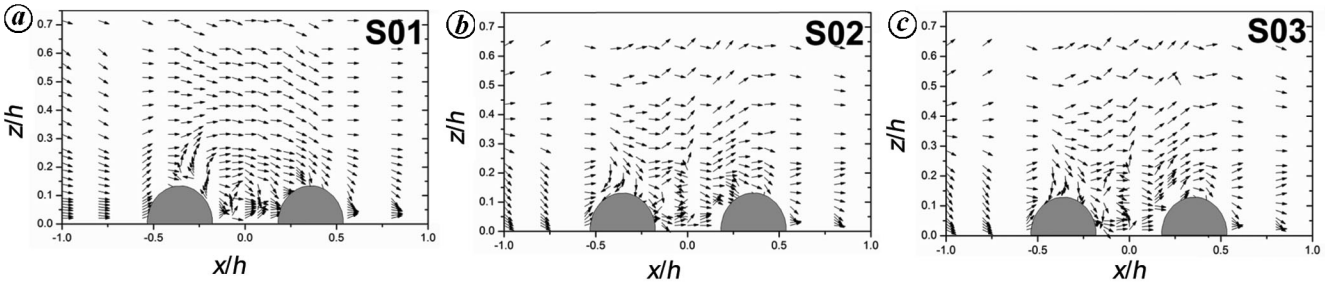

Figure 3. Mean velocity ($\overline{u}$ and $\overline{w}$) vector plot over two inline hemispheres in the *uw*-plane for (***a***) case S01, (***b***) case S02 and (***c***) case S03.

(= 0.042 cm) were achieved after comparing the log-law equation (eq. (2)) with the suitable equation of the obtained velocity data of plane bed. The normalized longitudinal $\hat{u}(=\overline{u}/u_*)$ and vertical $\hat{w}(=\overline{w}/u_*)$ mean velocities, Reynolds shear stress $uw^+(=-\overline{u'w'}/u_*^2)$, longitudinal $u^+(=u_{\text{rms}}/u_*)$ and vertical w^+ $(=w_{\text{rms}}/u_*)$ turbulence intensities are in agreement with the earlier studies of Nezu and Rodi[14], and Nezu and Nakagawa[15] for velocity measurement on the hydraulically rough bottom wall.

However, for couple interaction between current and waves; the instantaneous velocities are demarcated in the following form[4]

$$u(t)=\overline{u}+\tilde{u}(t)+u',\ w(t)=\overline{w}+\tilde{w}(t)+w', \tag{3}$$

where $\tilde{u}(t)=\langle u(t)\rangle-\overline{u}$, $\tilde{w}(t)=\langle w(t)\rangle-\overline{w}$, and the tilde, bar and prime notations represent the wave-induced, time-averaged and fluctuating velocity components respectively. Here, the wave-driven velocity $\tilde{u}(t)$ is achieved after subtraction between the time-averaged velocity $\overline{u}$ and phase-averaged longitudinal velocity $\langle u(t)\rangle$. Following a similar procedure, phase-averaged vertical velocity $\langle w(t)\rangle$ was determined.

Figure 2 *a* and *b* shows the longitudinal mean velocity over the flat surface at 10, 11 and 12 m downstream from the inlet of the channel. It can be observed that all the data collapse on each other and follow a similar pattern, which signifies the fully developed flow within the test section. Moreover, the vertical distributions of longitudinal mean velocity appear with the standard log-law[15]. Figure 2 *c*–*e* shows the distribution of Reynolds shear stress across z/h for the selected locations V3, V5 and V8. It can be perceived from this figure that the shear stress values are significantly reduced due to superimposed wave compared to only current flow at these measuring locations.

The mean velocity vector ($\overline{u}$ and $\overline{w}$) plot in the *uw*-plane over two inline hemispheres for three different cases, viz. S01, S02 and S03 is shown in Figure 3 for a clear view of the flow field. Here S01 refers to current only, S02 to frequency of wave $f = 1$ Hz, and S03 for $f = 2$ Hz. Figure 3 reveals that velocity vectors are almost parallel to the bed at the upper region of the middle wake zone ($x/h = 0$, Figure 3 *a*, S01). Whereas the velocity vectors shows a significant upward motion for wave-induced cases ($x/h = 0$, Figure 3 *b* and *c*, S02 and S03 respectively) at that particular location. Further, turbulence strength is characterized by parameters such as shear stress and intensity. These parameters took maximum magnitude at the cavity region and just downstream of the hemispheres at the relative flow depth $z/h = 0.07$ for only current flow and wave-current coexisting cases. Greater turbulence strength is characterized by the region of removal and suspension of sediment particles. Turbulence strength decreases as the measurement locations move towards the downstream hemisphere, which results in the settlement of sediment particles. In addition, negative contribution of

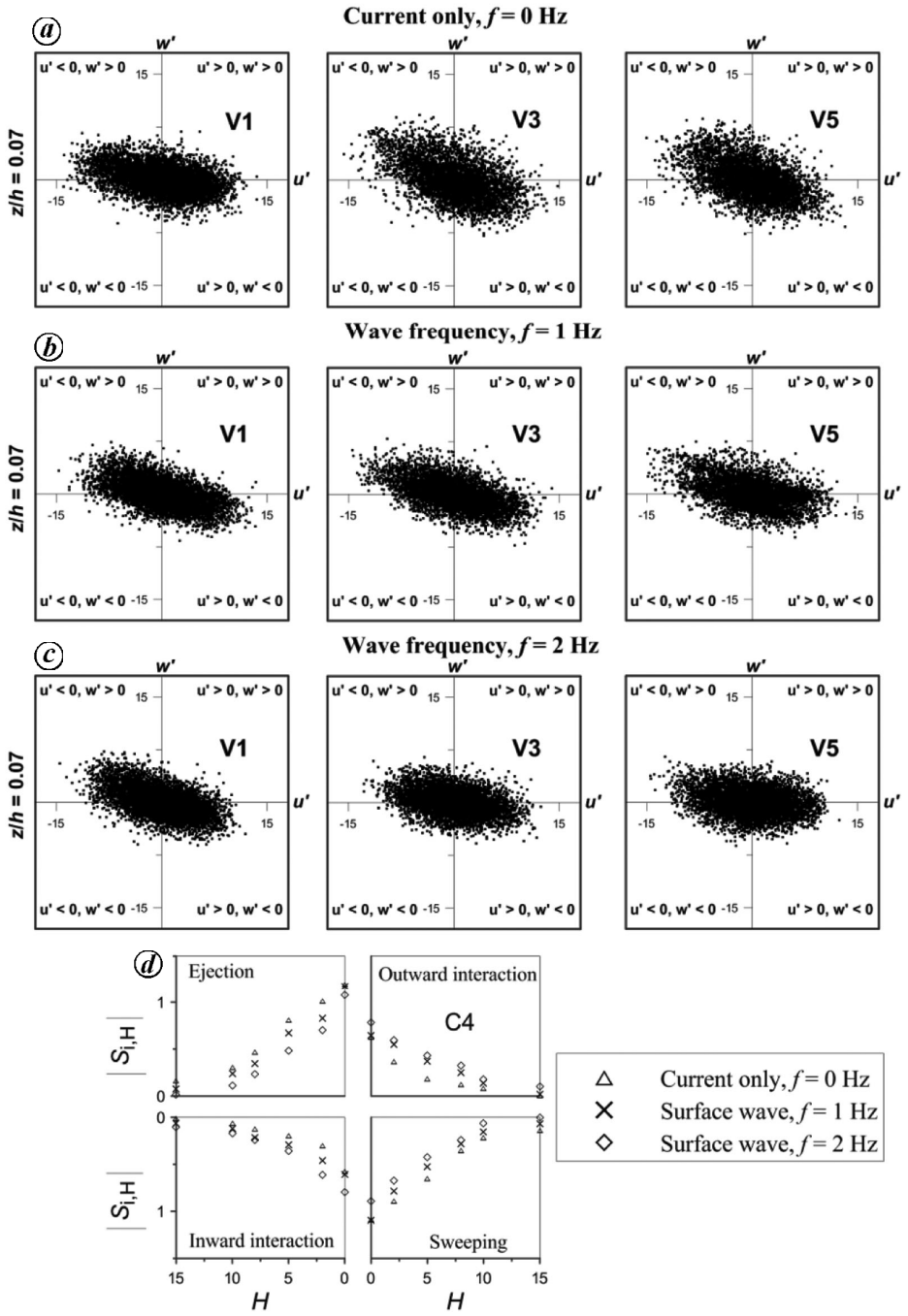

Figure 4. u'–w' scatter plots for (***a***) only current flow ($f = 0$ Hz), (***b***, ***c***) joined wave frequencies ($f = 1$ and 2 Hz) cases, and (***d***) stress fraction, $|S_{i,H}|$ and hole size H for only current flow and joined wave frequencies cases ($f = 1$ and $f = 2$ Hz).

shear stress value was observed at the cavity and downstream region of the hemispheres close to the bottom wall for associated wave–current cases as well as only current flow case, which attributes outward flux of momentum[11].

Turbulent bursting structure

The normalized Reynolds shear stress values uw^+ and $\langle uw^+ \rangle$ are maximum at the top of the hemispheres and thus to determine the distribution of different events a point $z/h = 0.07$ is chosen. The $u'w'$ scatter plots are presented in Figure 4 *a–c* for isolated current flow and mixed wave–current cases respectively, for the measuring sections V1, V3 and V5. Figure 4 *a–c* shows that most of the points drop in the second and fourth quadrants for isolated current flow and mixed wave–current cases for these measuring locations that correspond to the ejection-sweep bursting events. Comparisons of wave–current cases with current-only cases provide evidence that events in the wave–current flow are more scattered

irrespective of the quadrant. However, there is a notable difference in the shape of the scatter plot for the measuring location V1 (Figure 4 *a*), wherein it is observed that the plots for V3 and V5 are much more asymmetric compared to V1 for the current-only case. A similar increase in the spread of the scatter plot is observed on the superposition of wave. In general, contributions of ejection and sweep are higher, whereas inward and outward interactions are suppressed. In contrast, for $f = 2$ Hz (verticals V3 and V5), the scatter plots form a cloud with more coverage of all four quadrants, suggesting turbulence be closer to isotropic[16]. Also, it is observed from Figure 4 *a* (V1) that the formation of a cloud is similar to that for Figure 4 *c* (V5), which may be signifying the recirculation region behind (downstream) the hemisphere modulated due to the superimposed wave, and shows similar pattern as obtained in the upstream location for the current-only case. Figure 4 *d* shows the stress fraction as a function of hole size H (computed in a similar way as shown in Barman *et al.*[11]). Note that we have computed the stress fraction for all the locations and cases. For brevity, stress fraction for V3 at $z/h = 0.2$ is presented here (Figure 4 *d*). As shown in Figure 4 *d* the allowance of ejection and sweep contributions to the total shear stress is large for all H values at this particular position. This phenomenon depicts that the superimposed wave significantly modulates the turbulent structures at this location.

Distribution of probability density function

Each component of turbulent flow velocities at any point is a random variable. Its behaviour can be described by a PDF, which may be distinguished through distinct order of statistical moments. The nth order mathematical moment for longitudinal velocity components can be demarcated as[17]

$$E[u'^n] = \int_{-\infty}^{\infty} u'^n p(u') \mathrm{d}u', \tag{4}$$

where E [ ] represents the expected value, $p(u')$ is the PDF of random variable u' and n (= 1, 2, 3. . . .) is the nth order statistical moment. The ergodic progression of stationary time-series data E [u'^n] is interpreted in the following manner

$$E[u'^n] = \overline{u'^n} = \lim_{T\to\infty} \frac{1}{T} \int_{t_0}^{t_0+T} u'^n \mathrm{d}t, \tag{5}$$

where the overbar represents a time-averaged sense, $t = t_0$ is the onset time of the measured data, and T is the time period of the acquired data series.

The PDF of longitudinal velocity components was determined for particular vertical sections V1, V3, V5 and V7 at several z/h values. Figure 5 *a–c* shows the PDF of velocity fluctuations estimated at $z/h = 0.07$, 0.14 and 0.61 respectively. Figure 5 *a* shows that the longitudinal velocity component follows a Gaussian distribution at the upstream of the front hemisphere at location V1 close to the bottom wall at $z/h = 0.07$ for both only current and joined wave–current flows. At the wake region, for vertical locations V3 and V5 (Figure 5 *a*), the shape of all PDF profiles is platykurtic for interactions of wave–current and only current flows at $z/h = 0.07$. It can be discerned from Figure 5 *a* that the velocity fluctuation is two times greater for the vertical sections V3 and V5 and the peak value of PDF reduces near about 22–27% compared to the vertical location V1 at $z/h = 0.07$. At further downstream location V7 of the second hemisphere (Figure 5 *a*), a similar spread of velocity fluctuation is observed at the positive axis as that of location V1; and also the negative velocity fluctuation spread is similar for locations V3 and V5. Figure 5 *b* shows that the PDF profile is negatively skewed for the sections V1, V5 and V7 at $z/h = 0.14$ for couple interactions of wave–current and only current flow cases, except for the vertical V3 where the profile is symmetric. At $z/h = 0.14$, similar crest values of PDF are obtained between coexisting wave–current and only current flows. It can be anticipated from Figure 5 *c* that the shape of all PDF profiles is leptokurtic for the current-only case. Moreover, for the relative depth $z/h = 0.61$, the crest value of PDF is more tapering for only current flow in comparison with wave-induced cases. For wave frequency $f = 2$ Hz, two crest values of PDF are found at $z/h = 0.61$. On the other hand, a single crest value is attained for $f = 1$ Hz case. Two peaks of PDF depicts the bimodal nature for $f = 2$ Hz; this may signify that the superimposed surface wave modulates the distribution of velocity fluctuations and redistributes them in a higher scale (the probability of occurrence of velocity fluctuations is smaller around the zero mean). Further, this crest value is larger for frequency $f = 1$ Hz in comparison to $f = 2$ Hz for all measuring verticals. Here, root mean square (rms) and third and fourth-order moments for the longitudinal velocity component are estimated as

$$u_{\mathrm{rms}} = \sigma = \sqrt{\overline{u'^2}},\ \beta_1 = \overline{u'^3}/\sigma^3,\ \beta_2 = (\overline{u'^4}/\sigma^4) - 3. \tag{6}$$

The PDF and its statistical characteristics of non-dimensional stream-wise velocity fluctuation (scaled by rms value) were calculated using eq. (6); Table 1 presents the results. This table may be used for data validation for future numerical and experimental studies.

Distribution of turbulent eddies

Based on the presented results and discussion, it may noted that the interacting wave–current energy considerably modulates the eddy formation into flow field around

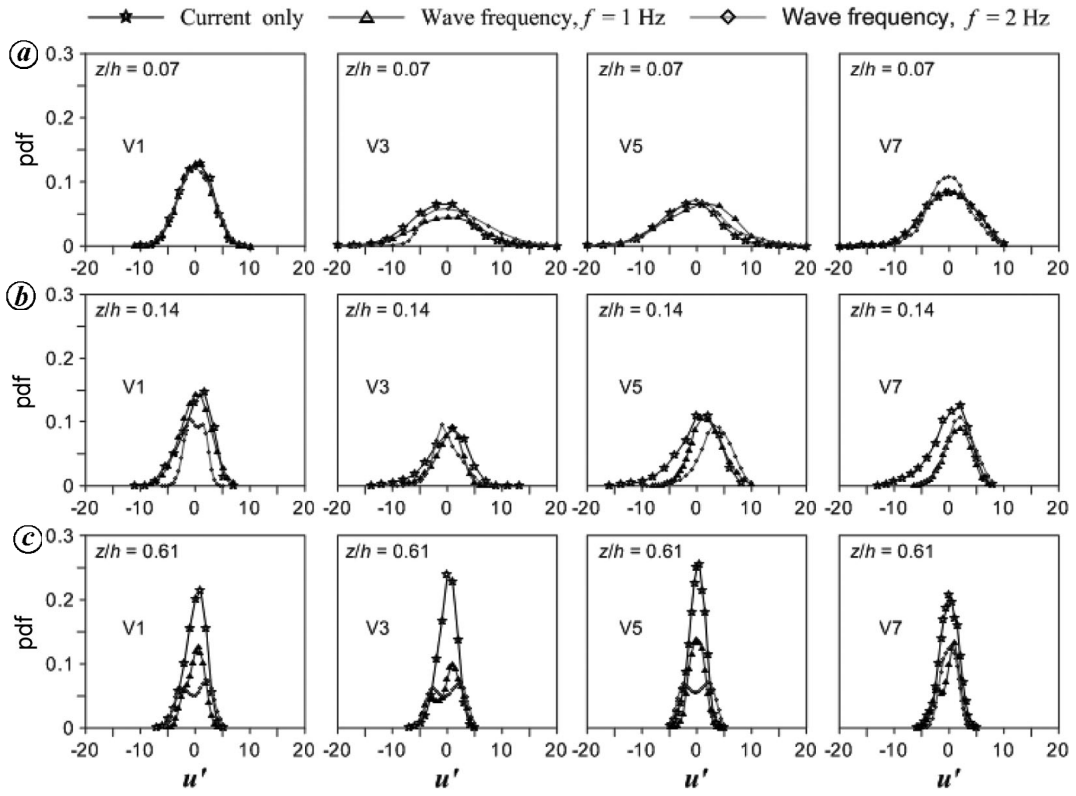

Figure 5. Distributions of probability density function (PDF) of longitudinal velocity components for only current flow (f = 0 Hz) and joined wave frequency (f = 1 and 2 Hz) at (***a***) z/h = 0.07, (***b***) z/h = 0.14 and (***c***) z/h = 0.61 for the locations V1, V3, V5 and V7.

the hemispheres. The quadrant analysis shows that the superimposed wave energy weakly modulates the recirculation zone, while it significantly modules at the upper position ($x/h = 0$, $z/h = 0.2$, V3) of the recirculation region. To recognize the behavioural pattern of eddy scale created by instantaneous longitudinal velocities, wavelet technique is presented here. Wang *et al.*[10] showed that the wavelet procedure of random velocity signals provides detailed information on the different eddy scales with their connected incidence frequencies.

However, for higher Reynolds number flow, the lengths of the eddy scale demonstrate a spacious range of spectral frequency band. Wavelet technique represents longitudinal velocity time-series data in the pseudo-frequency (f_{ps}) range. In the wavelet analysis of a velocity signal, the eddy scale to its occurrence frequency is connected for evaluation of the central frequency, f_c using the relationship

$$f_{ps} = \frac{f_c}{d\Delta},$$

where d and Δ are the eddy scale and sampling period (Hz) respectively. The time information can be captured through the short-time Fourier transform process, while interval of the time window is constant for this. However, continuous wavelet transforms of the fluctuating time series $s(t)$ may be interpreted along the family of wavelet functions[10] and is defined as

$$\bar{\omega}(l, d) = \frac{1}{\sqrt{d}} \int_{-\infty}^{\infty} s(t)\psi^*\left(\frac{t-r}{d}\right)\mathrm{d}t, \tag{7}$$

where $\bar{\omega}$, l, d and ψ are the wavelet coefficient, time or space location, wavelet scale and mother wavelet function respectively, while * signifies the conjugated value[10]. Li and Nozaki[18] specified that an eddy conceivably takes a function of frequency scale and time given by the wavelet coefficient. Also, the Morlet wavelet transform is used to characterize the eddy scales with regard to the magnitudes of wavelet coefficients.

It is important to note here that the instantaneous velocity signal without phase averaging is plotted in Figure 6 *a* and *d* as well as *g* and *j*, and is presented here to clearly visualize of the raw time series data. The wavelet transformation is performed for the associated velocity fluctuations of the same instantaneous velocity component at a particular measuring point. Figure 6 *c* and *i* depicts the fast Fourier transform (FFT) output for the instantaneous longitudinal velocity fluctuations and is compared with the pseudo-frequency of occurrence of different eddies scales. Figure 6 *b* shows the contour

Table 1. Values of mean (μ), standard deviation (σ), coefficient of skewness (β_1) and kurtosis (β_2) of longitudinal velocity fluctuations at z/h = 0.07, 0.14 and 0.61

Parameters		z/h = 0.07			z/h = 0.14			z/h = 0.61		
		Current only	f = 1 Hz	f = 2 Hz	Current only	f = 1 Hz	f = 2 Hz	Current only	f = 1 Hz	f = 2 Hz
V1	μ	0.004	–0.0008	0.0006	0.005	–0.0004	0.03	0.003	0.0001	0.02
	σ	2.85	2.9	5.7	2.7	2.7	2.4	1.88	1.5	2.2
	β_1	–0.09	–0.11	0.002	–0.3	–0.15	–0.29	–0.45	–0.28	–0.34
	β_2	–1.5	–0.06	–2.03	–1.4	–0.18	–1.3	–0.05	–0.45	–0.76
V3	μ	–0.62	–0.005	0.8	–0.12	0.9	0.0001	–0.009	0.0001	0.0003
	σ	5.1	5.7	5.5	3.7	3.05	2.4	1.6	1.2	2.5
	β_1	–0.08	–0.09	0.29	–0.25	0.26	0.09	–0.46	–0.06	–0.07
	β_2	–1.9	–2.1	–1.7	–1.93	–1.92	–1.45	0.17	–0.43	–1.14
V5	μ	–0.63	0.02	0.038	–0.007	0.9	0.1	–0.006	0.0003	0.008
	σ	5.3	4.2	6.1	3.8	2.3	4.3	1.5	1.7	2.4
	β_1	–0.3	–0.13	0.09	–0.35	0.04	0.84	–0.68	–0.42	–0.02
	β_2	–1.9	–1.24	–1.3	–1.2	–1.4	–1.6	2.7	–0.55	–1.09
V7	μ	–0.024	0.0002	0.003	–0.003	0.0004	0.08	–0.019	0.006	0.0001
	σ	4.4	3.1	3.6	3.5	1.6	3.1	1.7	2.4	1.4
	β_1	–0.09	–0.06	0.02	–0.46	–0.08	0.85	0.46	–0.08	–0.1
	β_2	–1.7	–0.33	–0.16	–0.74	–0.6	–1.3	2.1	–1.1	–0.47

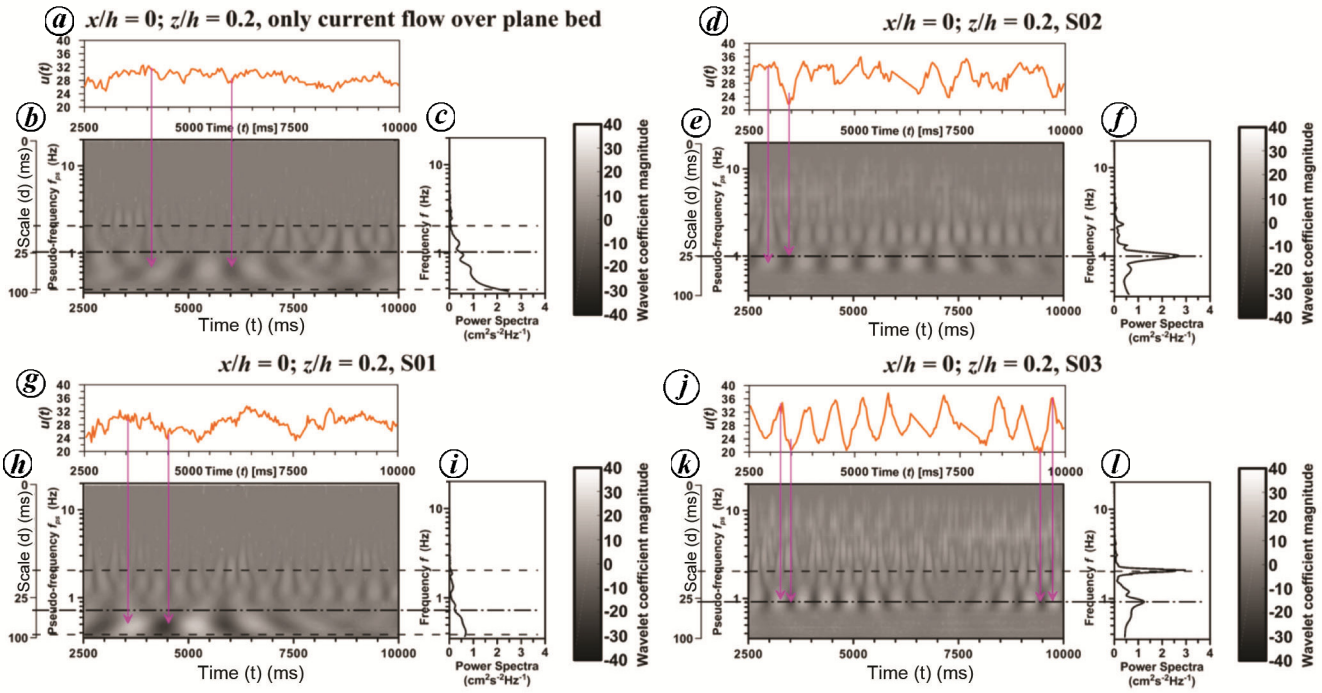

Figure 6. Plots of (***a***, ***d***) instantaneous longitudinal velocity time series; (***b***, ***e***) contours of wavelet coefficient; (***c***, ***f***) output of fast Fourier transform (FFT) for current-only flow over smooth and hemispheres bed; and (***g***, ***j***) instantaneous longitudinal velocity time series; (***h***, ***k***) wavelet coefficient contours; (***i***, ***l***) output of FFT for S02 and S03 cases at z/h = 0.2, x/h = 0 for the location V3.

representation of wavelet coefficients for current-only flow over plane bed at z/h = 0.2, x/h = 0. While Figure 6 *e* shows the contour illustration of wavelet coefficients for current-only flow over two inline hemispheres at z/h = 0.2, x/h = 0, V3.

It should be pointed out that the energy-containing eddies are organized into the pseudo-frequency range 0.35–0.7 Hz at z/h = 0.2, x/h = 0 (S01). A smaller frequency band (f_{ps} = 0.35–0.7) for S01 compared to the current-only flow over plane bed (f_{ps} = 0.35–1) case is evident. This reduction of the frequency band could be due to the generation of recirculating eddies at the hemisphere wake region.

Figure 6 *h* displays the contour of wavelet coefficients for wave–current combined flow (f = 1 Hz, S02) over

two inline hemispheres at $z/h = 0.2$, $x/h = 0$, V3. It is evident from Figure 6 *h* that the maximum energy containing eddies for wave–current combined flow (S02) over the hemispheres at $z/h = 0.2$, $x/h = 0$ have a pseudo-frequency $f_{ps} = 1$ Hz. It is important to note that the formation of more energetic eddies from the interaction of surface wave ($f = 1$ Hz) plays a significant role in modulating the eddy structures. Also, a high peak is observed in the output of FFT for $f = 1$ Hz (Figure 6 *i*). Furthermore, it is observed that some energetic eddies are concentrated at the energy-containing region $f_{ps} = 1$–3 Hz. These results demonstrate that the combined effect of the superimposed waves and hemispheres is capable of modulating the turbulent flow structures at the upper region of the recirculation zone ($z/h = 0.2$, $x/h = 0$). Figure 6 *k* depicts the contour of wavelet coefficients for wave–current combined flow ($f = 2$ Hz, S03) over two inline hemispheres at $z/h = 0.2$, $x/h = 0$, V3. It is interesting to observe that the energy containing eddies are well-organized in the range $f_{ps} = 1.8$–2.2 Hz, having a maximum peak at $f = 2$ Hz in the FFT output (Figure 6 *l*), which is the same frequency as that of superimposed waves. Some energy-containing high-scale eddies are also concentrated within the range of $f_{ps} = 0.35$–1.8 Hz with a surplus peak at $f = 1$ Hz in the FFT output (Figure 6 *h*). Figure 6 *a–f* and *g–l* reveals the prominent effects of the hemisphere and superimposed surface waves within the main flow field; these external forcing effects are capable of modulating the entire range of turbulent eddy scales within the flow field and play a prominent role in the distribution of different eddy scales in the frequency domain.

Conclusion

The interacting wave–current turbulent flow around the tandem hemispheres was analysed experimentally using ADV in tilting flume. This study of the near-bed wave–current dynamics over aligned hemispheres highlights the correspondence with coherent structures and formation of different eddies scale. In addition, PDFs are shown to characterize the oscillatory nature that affects the turbulent properties due to coexisting bluff body, current and waves dynamics. The longitudinal velocity fluctuation follows a Gaussian distribution for measuring section in front of the first hemisphere. Further, the crest value of PDF is sharper for current-only flow in comparison with combined wave–current cases at $z/h = 0.61$. For superimposed higher wave frequency (i.e. $f = 2$ Hz) at $z/h = 0.61$, two crest values of PDF were observed, while for the $f = 1$ Hz case, a single crest value was observed. The external forcing effects of the hemisphere and superimposed surface waves within the main flow field modulate the entire range of turbulent eddy scales and play a major role in the modulation of distribution of different eddy scales in the frequency domain. Therefore, statistical results have been used for verification of various numerical models, prediction of velocity and turbulence aspect due to couple dynamics of wave–current flow.

1. Ferrier, G. A. and Carpenter, R. C., Sub-tidal benthic heterogeneity: flow environment modification and impacts on marine algal community structure and morphology. *Biol. Bull*., 2009, **217**, 115–129.
2. Van Hoften, J. D. A. and Karaki, S., Interaction of waves and a turbulent current. In Proceedings of the 15th International Conference on Coast Engineering, ASCE, New York, 1976.
3. Kemp, P. H. and Simons, R. R., The interaction of waves and a turbulent current: waves propagating with the current. *J. Fluid Mech.*, 1982, **116**, 227–250.
4. Umeyama, M., Reynolds stresses and velocity distributions in a wave–current coexisting environment. *J Waterw. Port, Coastal Ocean Eng.*, 2005, **131**(5), 203–212.
5. Nikora, V. I., Goring, D. G. and Biggs, B. J. F., Some observation of the effects of micro-organisms growing on the bed of an open channel on the turbulence properties. *J. Fluid Mech.*, 2002, **450**, 317–341.
6. Agelinchaab, M. and Tachie, M. F., Open channel turbulent flow over hemispherical ribs. *J. Heat Fluid Flow*, 2006, **27**, 1010–1027.
7. Farge, M., Wavelet transforms and their applications to turbulence. *Annu. Rev. Fluid Mech.*, 1992, **24**, 395–457.
8. Szilagyia, J., Parlangeb, M. B., Katul, G. G. and Albertson, J. D., An objective method for determining principal time scales of coherent eddy structures using orthonormal wavelets. *Adv. Water Resour.*, 1999, **22**(6), 561–566.
9. Niu, J. and Sivakumar, B., Scale-dependent synthetic stream flow generation using a continuous wavelet transform. *J. Hydrol.*, 2013, **496**, 71–78.
10. Wang, H., Lee, S., Hassan, Y. A. and Ruggles, A. E., Laser-Doppler measurements of the turbulent mixing of two rectangular water jets impinging on a stationary pool. *Int. J. Heat Mass Transf.*, 2016, **92**, 206–227.
11. Barman, K., Debnath, K. and Mazumder, B. S., Turbulence between two inline hemispherical obstacles under wave–current interactions. *Adv. Water Resour.*, 2016, **88**, 32–52.
12. Barman, K., Debnath, K. and Mazumder, B. S., Higher-order turbulence statistics of wave–current flow over a submerged hemisphere. *Fluid Dyn. Res.*, 2017, **49**, 025504.
13. Roy, S., Samantaray, S. S. and Debnath, K., Study of turbulent eddies for wave against current. *Ocean Eng.*, 2018, **150**, 176–193.
14. Nezu, I. and Rodi, W., Open-channel measurement with a laser Doppler anemometer. *J. Hydraul. Eng*., 1986, **112**(5), 335–355.
15. Nezu, I. and Nakagawa, H., *Turbulence in Open-Channel Flows* (ed. Balkema, A. A.), CRC Press, Rotterdam, The Netherlands, 1993.
16. Pokrajac, D. and Manes, C., Components of the spatially-averaged turbulent stress in open channel flows over rough beds. *River Flow*, Dittrich, koll, Aberle and Geisenhainer, 2010.
17. Czernuszenko, W. and Rowinski, P. M., Shear stress statistics in a compound channel flow. *Arch. Hydro-Eng. Environ. Mech.*, 2008, **55**(1–2), 3–27.
18. Li, H. and Nozaki, T., Wavelet analysis for the plane turbulent jet. *JSME Int. J. Ser. B*, 1995, **38**(4), 525–531.

ACKNOWLEDGMENTS. We thank the Department of Science and Technology, Government of India for financial support (File No. EMR/2015/000266).

Received 5 May 2019; revised accepted 24 February 2020

doi: 10.18520/cs/v118/i12/1922-1929